Effect of air on granular size separation in a vibrated granular bed

Matthias E. Möbius,[1] Xiang Cheng,[1] Peter Eshuis,[1,*] Greg S. Karczmar,[2] Sidney R. Nagel,[1] and Heinrich M. Jaeger[1]
[1]*The James Franck Institute and Department of Physics, The University of Chicago, Chicago, Illinois 60637, USA*
[2]*Department of Radiology, The University of Chicago, Chicago, Illinois 60637, USA*
(Received 25 February 2005; published 22 July 2005)

Using high-speed video and magnetic resonance imaging (MRI) we study the motion of a large sphere in a vertically vibrated bed of smaller grains. As previously reported we find a nonmonotonic density dependence of the rise and sink time of the large sphere. We show that air drag causes relative motion between the intruder and the bed during the shaking cycle and is ultimately responsible for the observed density dependence of the risetime. We investigate in detail how the motion of the intruder sphere is influenced by size of the background particles, initial vertical position in the bed, ambient pressure, and convection. We explain our results in the framework of a simple model and find quantitative agreement in key aspects with numerical simulations to the model equations.

DOI: 10.1103/PhysRevE.72.011304 PACS number(s): 45.70.−n, 64.75.+g, 83.80.Fg

I. INTRODUCTION

Granular size separation is one of the most prominent phenomena in granular physics [1–3]. When a granular mixture is agitated via an external driving force, grains of different sizes separate into distinct regions of the container. This behavior sets granular materials apart from ordinary fluids which typically mix to increase entropy. A key reason is that granular media are far from thermal equilibrium, and that therefore the dynamics set up by the driving force govern their behavior. The phenomenon of granular size separation is well known. It manifests itself in a wide array of granular systems such as chute flows, avalanches and rotating drums [4–9].

Here we concentrate on a vertically vibrated bed in which a large spherical object, the "intruder," is embedded. The excitation typically causes the intruder to rise to the top of the bed, which is commonly referred to as the Brazil nut effect [10]. However, the detailed behavior is more complex. In particular the rate of rising is strongly density dependent and in some experiments light intruders have been found to sink [11,12]. Efforts to identify the underlying mechanism for the intruder motion have been stymied by the need to account for this wide variety of behaviors [13].

Until recently, the rising or sinking of an intruder has been treated as distinct phenomena. Although the interstitial fluid, typically air, has been shown to strongly influence this density dependent behavior of the intruder [12,14–16], the details of how it acts and whether it is the cause of this behavior have only been resolved recently [17]. While some reports have suggested that air is unimportant [11,18–21], others acknowledged its role in determining the intruder motion [12,14–17,22,23], but gave conflicting explanations. There have also been studies of closely related systems with multiple intruder, quasi-2D and bi-disperse systems [20,22,24–28].

This paper presents a systematic study of the effect of air on size separation in a three-dimensional, single intruder system and expands on a letter published earlier [17]. In general, size separation is caused by a variety of mechanisms (for a recent review, see [2]). Our system was chosen such that convection is the dominant transport mechanism in the absence of air. The separation mechanism is identified by employing magnetic resonance imaging (MRI) and high speed video. This allows us to map out in detail the dependence on system parameters and to establish a phase diagram that delineates the rising and sinking regimes. We then develop a model that can explain the key features of our results and also provides a unifying framework for seemingly conflicting or unconnected observations made in the literature. In particular, it shows the sinking and rising to originate from the same mechanism. We test this model through a simulation.

II. EXPERIMENTAL METHOD

All experiments were performed in an acrylic cylinder with an inner radius of $R=4.1$ cm. It was mounted on a VTS 100 electromagnetic shaker driven by a function generator that produced sinusoidal excitations ("taps") spaced one second apart. Figure 1 shows a sketch of the setup. The acceleration was measured in terms of the dimensionless peak to peak acceleration $\Gamma=a_{p\text{-}p}/2g$ and monitored by an accelerometer (PCB, model 353B03) attached to the vessel. The frequency of the excitations was typically fixed at $f=13$ Hz although we explored ranges between 10 and 30 Hz with no qualitative change in the results. We used different types of media to study the effect of density: glass ($\rho_m=2.5$ g/ml, MoSci Corp.), zirconium oxide ($\rho_m=3.8$ g/ml, Glen Mills), DVB resin ($\rho_m=1.0$ g/ml, Supelco), tapioca pearls ($\rho_m=1.2$ g/ml), poppy and rajagara seeds ($\rho_m=1.0$ and 1.2 g/ml, respectively). Here, ρ_m is the density of the bed particle *material*. The range of sizes we used as our bed medium was between 0.25 and 2.0 mm. The intruder particles were 25 mm hollow polypropylene spheres (Euro-Matic Plastics Inc.) filled with varying amounts of material such as lead shot to tune the density. The intruder was placed

*Permanent address: Physics of Fluids, Physics of Fluids Group, University of Twente, P.O. Box 217, 7500 AE Enschede, The Netherlands.

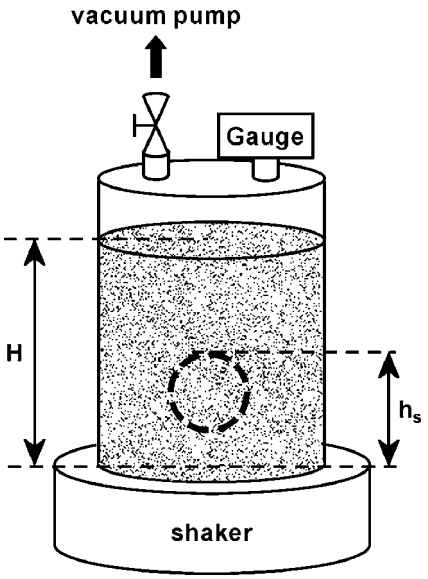

FIG. 1. Sketch of the setup. H is the total height of the bed and h_s the initial height of the intruder measured from its top. A vacuum gauge measures the background air pressure inside the cylinder.

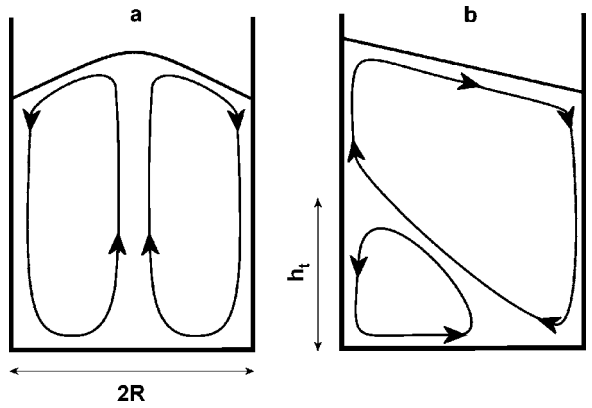

FIG. 2. Flow fields of the two observed convection patterns: (a) axisymmetric, wall-driven convection with a centered heap surface. Thin downstream at the walls and an upstream in the middle. (b) Asymmetric, air-driven convection with a slanted heap surface. Both images are to scale and represent flow patterns for shaken beds of $d=0.5$ mm glass media. Cell radius is $R=4.1$ cm and total bed height before shaking is $H=8.5$ cm. The height $h_t=4.5$ cm separates the regions of up and down flow of the particles at the wall.

along the cylinder axis at height h_s (Fig. 1). After each run, the cell was emptied and refilled to avoid compaction effects.

Two different cells were used: One had a smooth inner wall, the other was roughened by gluing glass beads to its surface, thus allowing us to study the effect of wall-driven convection on the intruder motion [29,30]. During the experiments the cylinder was closed with a lid that had a pressure gauge and quick release valve mounted on it. The cell could be evacuated to pressures between 0.13 and 101 kPa. The vacuum pump was then disconnected via the valve to avoid vibrations caused by dangling tubes.

A thin plastic straw attached to the intruder that extended above the bed surface enabled us to track the intruder motion inside the bed. We recorded the motion of the straw with a high-speed video camera to measure the intruder trajectory during the shaking cycle as well as the net displacement of the intruder after each tap. Measurements of the risetime with and without the straw did not show any difference within experimental accuracy.

Two different techniques were employed to probe the interior of the three-dimensional particle bed. One of them involved non-invasive magnetic resonance imaging (MRI). The bed was layered with MRI active poppy seeds and MRI passive rajagara seeds [17]. As a result, a MRI image of an axial cut through the bed shows a stack of bright and dark bands. After each tap and once the system has settled we take a MRI snapshot, imaging a vertical slice through the center. From the displacement of the bands between taps we can then deduce the flow field. While the size and density differences between the two types of seeds is small, it is not clear a priori that they do not matter. The poppy seeds are kidney shaped whereas the rajagara ones are more spherical, although both are of comparable size ($d \approx 0.7$ mm). In order to ensure that our MRI results are unaffected by these differences and hold for media other than seeds, we employed a second technique to visualize the inside of a bed of glass beads. In this technique, initially the bed was prepared with equally spaced layers of black and white glass beads. The flow field at later times was obtained by carefully backfilling the cell with water, freezing it, and then cutting it along the central axis.

III. RESULTS AND DISCUSSION

A. Convective flow patterns

Since convection plays an important role in granular size separation in systems such as ours [29], we first investigated the convective flow. There are two types of convection patterns we observe—one is symmetric and the other asymmetric (Fig. 2). For glass media the symmetric roll is observed with $d > 0.5$ mm in the smooth cell and $d > 0.35$ mm in the rough cell. This is the well known wall-driven convection roll [29,30] that has a thin downstream region near the walls and a large upstream flow in the center of the bed [Fig. 2(a)]. Small background media, in which air effects are more pronounced due to the lower bed permeability, undergo the asymmetric convection despite careful leveling procedures. We found this asymmetric behavior for all glass media with diameters $d \leqslant 0.5$ mm in the smooth and $d \leqslant 0.35$ mm in the rough cell. In this case a surface instability caused by air flow dominates the wall-driven convection and a large convection roll spanning the entire diameter of the cell sits on top of a small one [Fig. 2(b)]. The asymmetric roll tends to drive bed particles towards the wall at which point they either move downward or upward depending on their vertical position.

B. Density dependent intruder risetime

When an intruder is placed in the bed, it will typically rise upon shaking. For sufficiently small and light media in

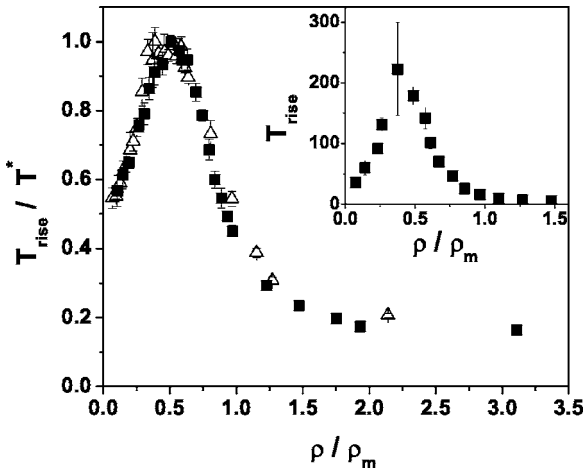

FIG. 3. Normalized risetime T_{rise}/T^* versus ρ/ρ_m for different background densities. T^* is the risetime at the peak. The size of the media is $d=0.5$ mm, $h_s=4.5$ cm, $\Gamma=5$, and $f=13$ Hz, $H=8.5$ cm. Symmetric convection: (■), glass ($\rho_m=2.5$ g/ml); (△), zirconium oxide ($\rho_m=3.8$ g/ml) in rough cell. Inset: asymmetric convection, (■), DVB resin ($\rho_m=1.0$ g/ml) in smooth cell.

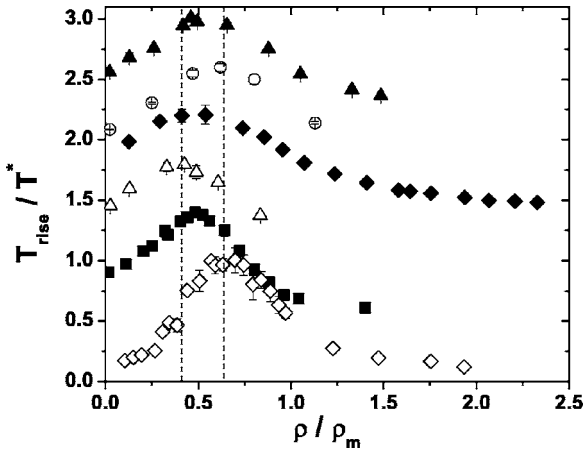

FIG. 4. Normalized risetime T_{rise}/T^* versus ρ/ρ_m for different excitation parameters, boundary conditions, interstitial gases and media. In all cases convection is symmetric and $H=8.5$ cm. For clarity, all the curves except (◇) have been shifted vertically with separation 0.4. The vertical dashed lines are at $\rho/\rho_m=0.41$ and 0.63, respectively. Unless stated otherwise, we used these standard parameters: rough cell, $R=4.1$ cm, $h_s=4.0$ cm, $d=0.5$ cm glass beads, $\Gamma=5$ and $f=13$ Hz. (■), standard conditions; (▲), $\Gamma=3$; (○), $R=6.0$ cm; (◆), poppy seeds $d=0.7$ mm; (△), ambient gas is helium ($\rho_{\mathrm{helium}}\approx\rho_{\mathrm{air}}/7$); (◇), $d=1.0$ mm, smooth cell, $h_s=4.5$ cm.

which air effects are important, the rate of rising strongly depends on the relative density between the intruder and the bed medium ρ/ρ_m.

Despite the two different flow patterns in the bed the behavior of the intruder is qualitatively the same in both the symmetrical and asymmetrical patterns as can be seen in Fig. 3. The plot shows the risetime as a function of the intruder density, where both axes have been rescaled with the convective risetime T^* and the density of the bed ρ_m, respectively. The nonmonotonic curves in Fig. 3 are typical for air-driven size separation [14–18]. Light and heavy intruders rise faster than those at intermediate density.

We define the density at the peak, ρ^*, to be the point at which the risetime T_{rise} is maximized or diverges as shown in later plots. In Fig. 3, $\rho^*/\rho_m\approx 0.5$. The curves correspond to different background densities of the same size ($d=0.5$ mm). Both the glass and zirconium oxide bed exhibit axisymmetric convection as depicted in Fig. 2(a), while the DVB medium does not, despite having the same size and thus the same permeability. However, due to its lower density it is more susceptible to air effects which causes the axisymmetric roll to go unstable and the convective flow becomes asymmetric as illustrated in Fig. 2(b). Instead of observing a peak at ρ^*/ρ_m, we find that the risetime diverges, since the convective flow drives the intruder with $\rho=\rho^*$ to the wall where it stays for long times (sometimes indefinitely). The inset to Fig. 3 shows the divergence at approximately the same relative density as the peak in the main panel. This means that ρ^*/ρ_m does not depend on the symmetry of the convective flow.

The ratio ρ^*/ρ_m is almost constant over a range of system parameters (Fig. 4). The density of the interstitial gas and the medium, the size and boundary condition of the cell and the excitation strength do not significantly influence the peak position. ρ^*/ρ_m always lies between 0.41 and 0.63. This range of peak positions agrees with recent results by other groups in similar systems [16,18]. Around the same relative density Yan *et al.* [12] furthermore observed a diverging risetime. However, in their system the intruder sank below that density.

C. Intruder motion and convective flow

Our previous MRI experiments established that intruders with density ρ^* move with the surrounding bed while light and heavy intruders rise faster than convection [17]. MRI is, however, limited to imaging bed particles that contain traces of water or oil, such as seeds. Therefore we checked this important assertion more generally for other particles, by freezing a water-saturated sample as explained earlier. Figure 5 shows axial cuts through the bed for three different density intruders. The results confirm the MRI data for poppy seeds [17]. At a density ratio $\rho/\rho_m\approx 0.5$, the intruder does not move with respect to its surroundings and follows the con-

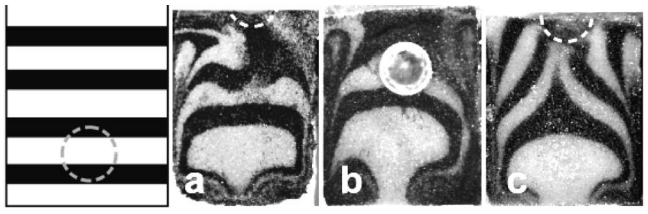

FIG. 5. Axial cuts through cell for three different density intruders. The bed has been cut after it was saturated with water and frozen. The bed medium consists of 0.5 mm glass beads, interleaved with black-colored layers. Left: sketch of original configuration. (a) $\rho/\rho_m=0.043$, 26 taps; (b) $\rho/\rho_m=0.5=\rho^*/\rho_m$, 26 taps; (c) $\rho/\rho_m=3.3$, 6 taps. In (a) and (c) the final intruder positions are denoted by a dotted circle. Sample (b) was cut with the intruder still inside the bed.

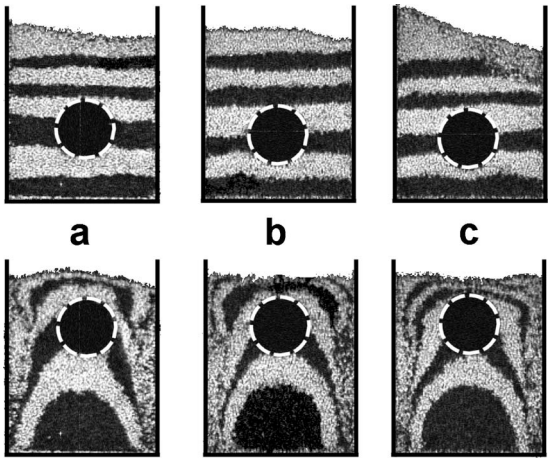

FIG. 6. Absence of density dependence in vacuum. The pictures are MRI images of axial cuts through the bed for different density intruders at $p=0.13$ kPa. System dimensions: $R=3.8$ cm, $H=4.2$ cm, and $D=1.6$ cm. The excitation parameters were $f=10$ Hz and $\Gamma=3$. Upper row shows initial configuration. Lower row shows system after 8 ± 1 taps. Column (a) $\rho/\rho_m=0.05$, (b) $\rho/\rho_m=0.45$, (c) $\rho/\rho_m=2.4$.

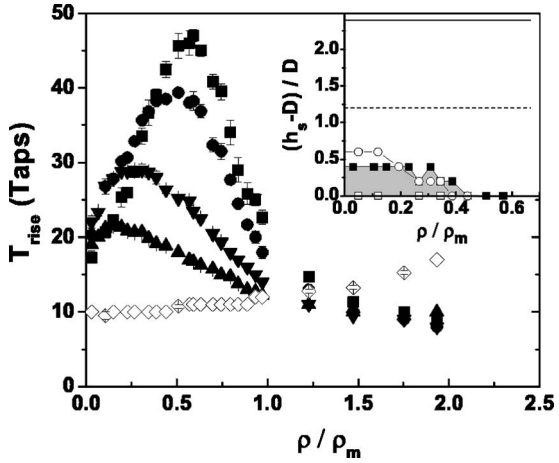

FIG. 7. Risetime curves at different pressures and the phase diagram in the rough cell. $\Gamma=5$, $f=13$ Hz, and $H=8.5$ cm. Intruder risetime $T_{\rm rise}$ versus ρ/ρ_m at different pressures P in the rough cell at $h_s=5.5$ cm: (■), 101 kPa; (●), 47 kPa; (▼), 13 kPa; (▲), 6.7 kPa; (◇), 0.13 kPa. Inset: Phase diagrams delineating the rising and sinking regimes for $d=0.5$ mm beds at various pressures P. Above each phase boundary, intruders rise. Shaded area shows the sinking regime at ambient pressure. Solid and dashed lines indicate total bed height and starting height, respectively. (■), 101 kPa; (○), 27 kPa; and (□), 0.13 kPa.

vective flow. It has not separated from the first black layer it was originally sitting on. The heavy intruder shows a characteristic wake below it and is well above the first black layer. Nearby particles are drawn under the sphere. The light intruder is also clearly displaced from its original position but does not exhibit the pronounced wake shown by the heavy intruder. This indicates different mechanisms for the light and heavy intruder by which they rise faster than convection. This behavior also holds for the asymmetrically convecting bed. Intruders near $\rho/\rho_m\approx0.5$ follow the convective flow that drives them towards the wall.

D. Effects of air and phase diagram

MRI images of intruders rising in an evacuated bed (Fig. 6) show that the density dependence of the risetime is due to the presence of air. Intruders with different densities all rise with the surrounding bed. There is no relative motion between the intruder and its vicinity. The only transport mechanism is global convection [14,15,17,29].

At atmospheric pressure, on the other hand, the air enables intruders which are lighter or heavier than ρ^* to rise faster than convection (Fig. 5). This result originates from the interaction between the bed, the intruder and the interstitial air which we will discuss later. However, this is not the only possible outcome. The *same* system can exhibit sinking behavior. This is one of our central results and is summarized in Figs. 7 and 8. These data show how pressure and initial vertical position in the bed determine whether the intruder moves up or down.

In order to test the influence of convection we performed the same experiments in rough and smooth cells, which differ in convection speed and flow pattern, keeping all other parameters the same. In both cases we used a 0.5 mm glass medium. The rough cell exhibits symmetric wall-driven convection. In the smooth cell convection is significantly reduced and the flow is asymmetric as depicted in Fig. 2(b). In Figs. 7 and 8 the initial starting height is just above the middle of the bed at $h_s=5.5$ cm. In both cases the curve either peaks or diverges at $\rho^*/\rho_m\approx0.5$. As the pressure is lowered ρ^*/ρ_m and the associated risetimes decrease. It is known from Kroll's work [31] that, due to air drag, the bed does not lift off as high as it would in vacuum. This has a direct consequence on the wall-driven convective flow. There is less shear with the side walls and thus, convection is reduced. As a result intruders rise faster in vacuum than in the presence of air. This leads to the shorter risetimes we observe at low pressures. In both cells the density at which the peak occurs decreases significantly at low pressures [17].

We also observe a transition between a rising and sinking regime in the smooth cell. Below a certain pressure intruders with densities below ρ^* sink. The resulting rise-sink time curve is shown in Fig. 8(b). The data resemble those found earlier by Yan *et al.* [12]. When the pressure is lowered even further the intruders rise again and the density dependence of $T_{\rm rise}$ vanishes.

This crossover between rising and sinking is not only controlled by pressure but also by the vertical position of the intruder in the bed. If the intruder is initially placed below a certain crossover height h_c it sinks. In general, h_c depends on several other parameters as well: The pressure P, the size of the medium d, the density ρ_m, the total height H, and the wall roughness.

In order to delineate the rising and sinking regimes, we map out phase diagrams in terms of the normalized starting height, $(h_s-D)/D$, and the normalized density, ρ/ρ_m (insets to Figs. 7 and 8, and main panel of Fig. 9). The lines connecting the data in these phase diagrams give the experimentally determined, normalized crossover height $(h_c-D)/D$.

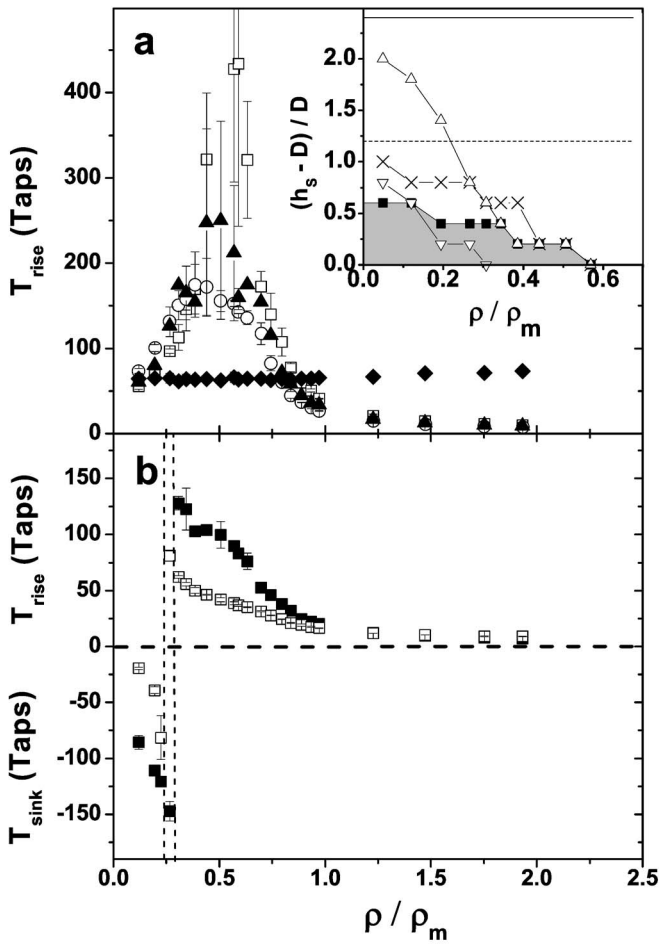

FIG. 8. Rise-sink time curves at different pressures and the phase diagram in the smooth cell. $\Gamma=5$, $f=13$ Hz, and $H=8.5$ cm. (a) Intruder risetime T_{rise} versus ρ/ρ_m at different pressures P in the smooth cell at $h_s=5.5$ cm: (□), 101 kPa; (▲), 40 kPa; (○), 27 kPa; (◆), 0.13 kPa. Inset: Phase diagrams delineating the rising and sinking regimes for $d=0.5$ mm beds at various pressures P. Above each phase boundary, intruders rise. Shaded area shows the sinking regime at ambient pressure. Solid and dashed lines indicate total bed height and starting height, respectively. (■), 101 kPa; (×), 27 kPa; (△), 2.7 kPa; (▽), 0.67 kPa in the smooth cell. (b) The divergent sinking regime. (■), 13.3 kPa with $\rho^*=0.28$ and (□), 2.7 kPa with $\rho^*=0.24$. Same conditions as in (a). The vertical dashed lines correspond to ρ^*.

Started above the lines, intruders rise, started at or below the lines they sink. The gray areas in the insets of Figs. 7(a) and 8(a) denote the sinking regimes at atmospheric pressure. As the pressure is lowered h_c initially increases and then drops. The intruders, regardless of their density, rise from the bottom of the cell ($h_c=D$) when $P<0.13$ kPa. In this regime air effects do not play any role. In the rough cell, h_c is lower and the pressure dependence not as pronounced as in the smooth cell. We believe that strong convection in the rough cell gives an upward bias and therefore lower crossover heights compared to the smooth cell. The difference between the rough and smooth cell might have another cause. Increased shear at the walls could cause bed dilation and therefore provide a shortcut for the air due to increased permeability.

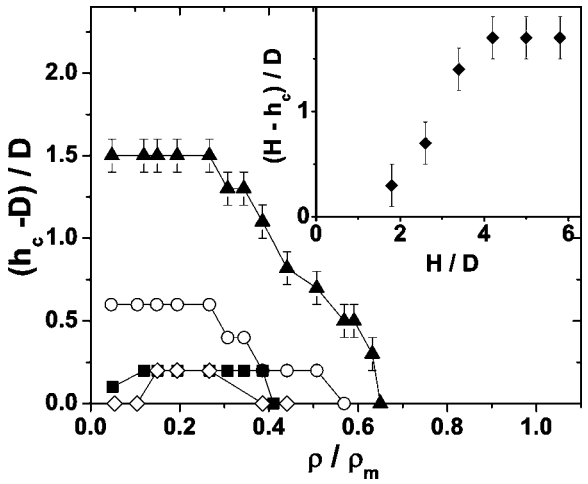

FIG. 9. Phase diagram for different sized glass media in the smooth cell at $P=101$ kPa. $\Gamma=5$, $f=13$ Hz, and $H=8.5$ cm. (▲), 0.25 mm; (○), 0.5 mm; (■), 1.0 mm; (◇), 2.0 mm. Inset: Crossover height h_c versus total height H normalized by D for 0.25 mm glass medium in the smooth cell.

This would lead to a decrease in air effects in the rough cell.

The sinking of the intruder is caused by pressure gradients across the bed exerting a net downward pull on the intruder [17]. Therefore, the phase diagram changes with the permeability of the bed, since the magnitude of the pressure gradient is inversely proportional to the permeability according to Darcy's Law. We can adjust the permeability k by changing the size of the background medium, since $k \propto d^2$. Figure 9 shows the phase diagram for glass beads of different sizes. As the medium size increases, the sinking regime shrinks. This is expected since in the limit of large permeability the pressure gradients are too weak to induce sinking. Indeed, we find that above $d=2$ mm all intruders rise with convection and air effects become negligible. The inset in Fig. 9 shows $(H-h_c)/D$ versus the normalized total height H/D. The curve saturates as H increases.

E. Size dependence

In the results shown so far, the relative size between the intruder and the medium, D/d, has been kept at 51. It is vital for understanding the effect to see whether the strong density dependence is still observed as D/d approaches 1. Figure 10(a) shows the size dependence of the risetime for different intruder densities at atmospheric pressure. Size affects the risetimes notably. Both size and density dependencies become less pronounced for smaller D/d. This might also explain the results of Huerta *et al.* [18]. They find the convective risetime to be faster than most intruder risetimes. However, they measured convection in the absence of intruders which is different from when an intruder is present. Figure 10(a) clearly shows that convection risetime in the absence of an intruder (dotted line) is lower than the risetime of the intruder at the peak ($\rho/\rho_m=0.47$). From our previous MRI measurements [17] and frozen-bed images (Fig. 5) we know that this intruder risetime reflects the actual convection time. We believe that the large sphere blocks air flow,

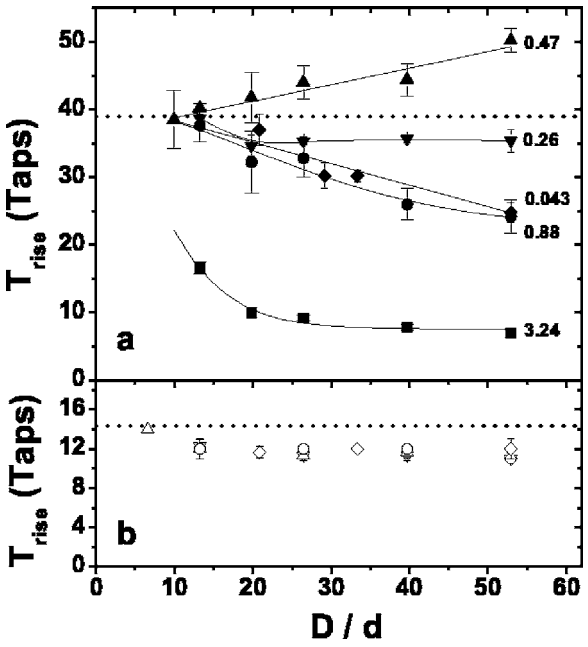

FIG. 10. Intruder risetime T_{rise} versus relative size D/d for different densities at two different pressures: (a) atmospheric pressure $P=101$ kPa and (b) low pressure $P=0.13$ kPa. $\Gamma=5$, $f=13$ Hz, $H=8.5$ cm, and $h_s=4.0$ cm. The numbers next to the line indicate the relative density. The dotted line indicates the convective risetime *without* the intruder. Relative densities in panel (b) are ($\diamond$), $\rho/\rho_m=0.043$; ($\triangledown$), $\rho/\rho_m=0.26$; ($\triangle$), $\rho/\rho_m=0.47$; ($\bigcirc$), $\rho/\rho_m=0.88$. The heaviest intruders ($\rho/\rho_m=3.24$) stop rising roughly one intruder diameter below the surface.

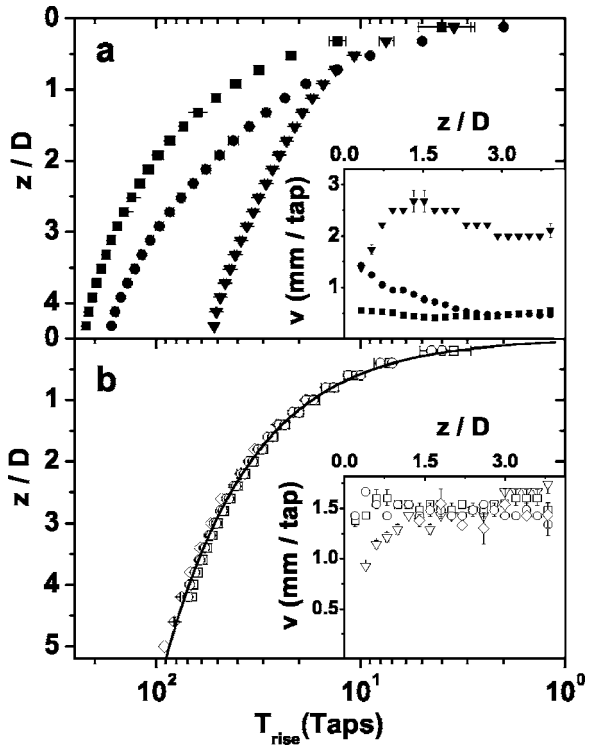

FIG. 11. Depth dependence of intruder risetime in 0.5 mm glass medium. Total bed height $H=13.5$ cm, $\Gamma=3.5$, and $f=13$ Hz. Upper panel (a): T_{rise} versus z/D for different density intruders ($D/d=50$) at atmospheric pressure. ($\bullet$), $\rho/\rho_m=0.043$; ($\blacksquare$), $\rho/\rho_m=0.52\approx\rho^*/\rho_m$; ($\blacktriangledown$), $\rho/\rho_m=3.3$. Inset shows the velocity at different depths. Lower panel (b): Same plot as above, but at $p=0.13$ kPa. ($\bigcirc$), $\rho/\rho_m=0.043$; ($\square$), $\rho/\rho_m=0.52\approx\rho^*/\rho_m$; ($\triangledown$), $\rho/\rho_m=3.2$; ($\diamond$), convection without intruder. Solid line is a linear fit with slope 0.058 tap^{-1}.

thereby decreasing permeability which in turn slows down convection. At relative sizes $D/d<10$ the influence of the intruder on the bed diminishes and risetime of the intruder at the peak approaches the convective risetime without the intruder. Therefore, at small D/d air-driven size separation becomes negligible and convection dominates [29].

At pressures below 0.13 kPa [Fig. 10(b)], the risetimes are nearly independent of ρ/ρ_m and D/d and are close to the convective risetime in the absence of an intruder. The slight increase in T_{rise} at low D/d might be due to geometric arching effects as discussed in [32–36]. Also, the heaviest intruder ($\rho/\rho_m=3.24$) does not surface at low pressures. It stops rising just below the surface and appears to sink back into the fluidized layer. At atmospheric pressure, the heavy intruders have a longer flight time than the bed due to their larger inertia so that the bed is already condensed when the sphere hits the surface. This explains why it does not sink back in as much as it does at low pressure when the upper surface is still fluidized at impact.

F. Intruder trajectories

In order to elucidate the mechanisms by which light and heavy intruders rise faster than convection, we tracked their positions during the ascent. Figure 11(a) shows the risetime as a function of depth for different density intruders at atmospheric pressure. The inset shows the displacement per tap versus depth. Deep in the bed the light intruder moves as fast as the intruder at the peak density ρ^*. It then speeds up as it approaches the surface. The heavy intruder is always faster, but slows down near the surface, because it falls back into the fluidized top layer at the end of the cycle. Below 0.13 kPa, the curves collapse and the only transport mechanism is convection [Fig. 11(b)]. This is consistent with the convective risetime equation $z(t)=\xi\ln(1+T_{\mathrm{rise}}/\tau)$ found by Knight *et al.* [30] given that in the present experiments the bed height H is comparable to the depth of the convection roll, ξ. This implies that $T_{\mathrm{rise}}\ll\tau$, leading to $z\approx(\xi/\tau)T_{\mathrm{rise}}$. The data in Fig. 11(b) are well fit with $\xi/\tau=1.5$ mm/tap (solid line).

Using high-speed video to image the trajectory of the intruder during one shaking cycle we arrive at a more detailed understanding of the mechanism by which the intruders rise or sink. Figure 12(a) shows the trajectories of intruders for three densities. The vertical lines delineate two parts of the shaking cycle. In part I, air flows down to the gap that opens up at the bottom of the cell [37,38]. In the second part, the gap starts to close and air has to leave the bed. At ρ^* the intruder has the smallest net upward displacement. The heavy intruder rises higher than all the others, as its inertia is large compared to air drag. Therefore, its net upwards displacement happens in part I. The light intruder on the other hand does not rise higher than the one at ρ^*. However, it

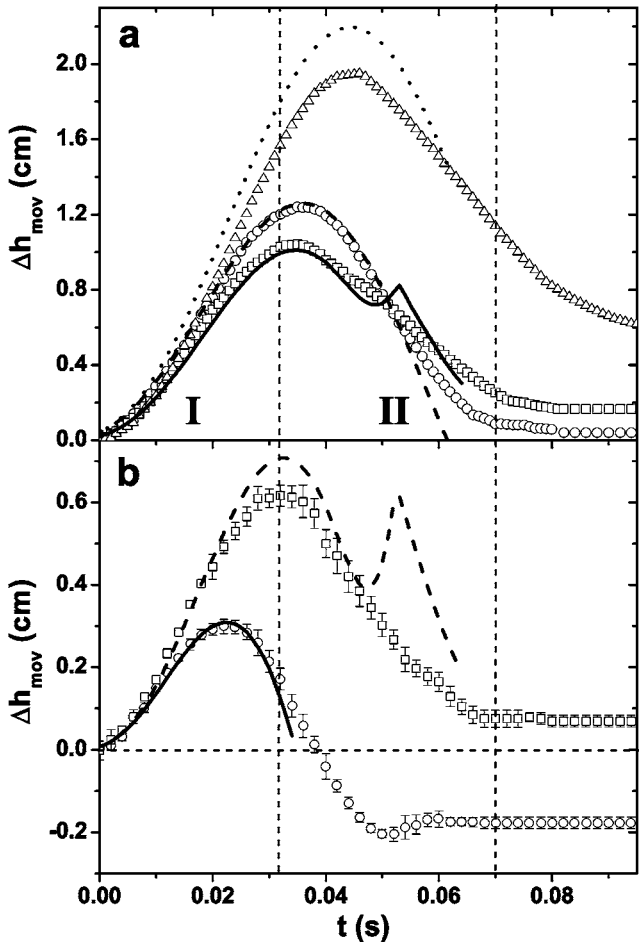

FIG. 12. Intruder displacement in the shaker frame. The vertical dashed lines delineate the part I and part II of the cycle (see text). (a) Three different densities with $h_s=7.0$ cm in the rough cell. (□), $\rho/\rho_m=0.043$; (○), $\rho/\rho_m=0.52\simeq\rho^*/\rho_m$; (△), $\rho/\rho_m=3.3$. The solid, dashed, and dotted lines are simulation results for trajectories of the light, medium, and heavy intruder (Sec. V). (b) Light intruder ($\rho/\rho_m=0.043$) in smooth cell rising at $h_s=6.5$ cm $>h_c$, (□), and sinking at $h_s=3.5$ cm $<h_c$, (○). The solid and dashed lines are the respective simulation results. The packing fraction was chosen to be $\phi=0.59$ and $\phi=0.63$ for the rough and smooth cell, respectively. For the sinking intruder in (b), the simulation was stopped at $t=36$ ms when the bed volume underneath the intruder hits the bottom of the cell.

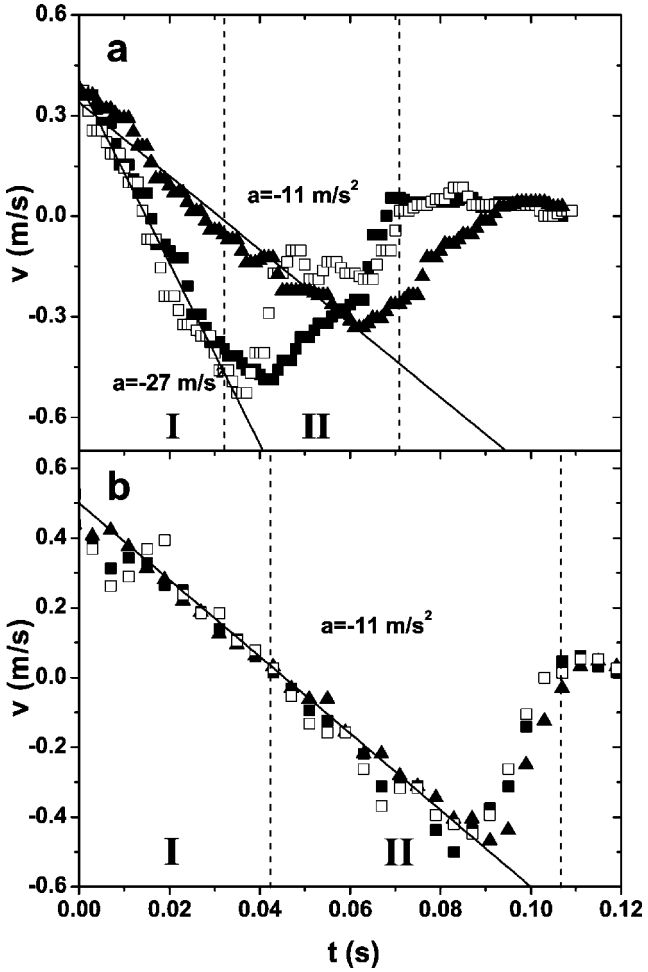

FIG. 13. Intruder velocity in the lab frame at: (a) atmospheric pressure $P=101$ kPa and (b) low pressure $P=0.13$ kPa. The vertical dashed lines delineate the part I and part II of the period (see text). Three different densities with $h_s=6.0$ cm in the rough cell. (□), $\rho/\rho_m=0.043$; (■), $\rho/\rho_m=0.52\simeq\rho^*/\rho_m$; (▲), $\rho/\rho_m=3.3$. The accelerations denote the slopes of the corresponding solid lines.

slows down in part II, leading to a higher *net upward* displacement than the intruder at ρ^*.

The velocity trajectories of the three intruders in the lab frame [Fig. 13(a)] show that the heavy intruder experiences little retardation. The slope of the velocity curve is close to $-g$ as denoted by the solid line throughout part I and II. It only slows down once the bed starts to condense after part II. Conversely, the lighter intruders are subject to a significant drag force as evident from their high downward acceleration: the first part of the velocity curves is well fit by the $-3g$ slope of the solid black line. They both slow down at the beginning of part II when the air flow reverses.

Figure 12(b) shows the trajectories for light intruders ($\rho\ll\rho^*$) above and below the crossover height. Both intruders are slowed down in part II by the escaping air. In part I, however, the sinking intruder does not rise as high as the ascending intruder which causes a net downward displacement after part II. This observation is crucial for understanding the underlying mechanism.

Several studies [11,18,20,21] have suggested that the right hand side of the peak is caused by inertia. In this model heavy intruders penetrate more easily through the bed which is held back by shear with the walls. In vacuum, where gravity and wall-shear are the only forces acting on the bed, our data for the intruder trajectories show no evidence of this. All intruders experience the same acceleration close to g during flight [Fig. 13(b)]. Therefore, the wall shear transmitted through the bed exerts only a small force on the intruder in the absence of air with little or no density dependence.

Figure 14 shows the light intruder trajectory for different depths in the lab frame. As in Fig. 12, the light intruder slows down in part II of the cycle and reaches a terminal velocity. There is a pronounced kink at the onset of the slowdown. The closer the intruder is to the surface the more it slows

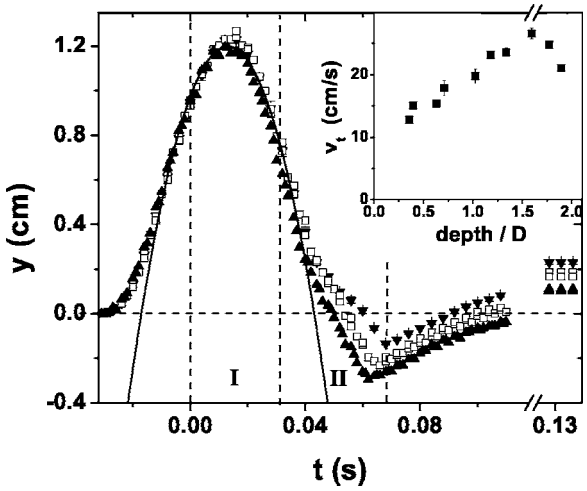

FIG. 14. Trajectory of light intruder ($\rho/\rho_m=0.043$) in the lab frame in $d=0.5$ mm glass medium at different depths in the rough cell. $\Gamma=5$, $f=13$ Hz. (▲), $h_s=4.0$ cm; (□), $h_s=5.5$ cm; (▼), $h_s=7.5$ cm. The black line is a parabola with acceleration $a=-27$ m/s^2. Inset: (■), terminal velocity versus depth.

down, which increases the upward displacement and is in agreement with our previous observation in Fig. 11. The inset shows how the terminal velocity decreases as the intruder nears the surface.

G. Air drag

In the following we look at the influence of the pressure gradients inside the bed on the motion of the intruder. These pressure gradients can be significant in vibrated beds [37]. To see its effect on the intruder motion we performed a simple experiment: Two intruders, one with $\rho \approx \rho^*$ and the other with $\rho \gg \rho^*$, were put on top of a bed. After tapping, the trajectories of the two intruders differ notably at atmospheric pressure. While the heavy intruder is visible throughout the cycle, the lighter one is "sucked" into the bed and disappears. At the end of the shaking cycle, the light intruder reappears, while the heavy one burrows into the bed due to its large inertia [39]. In vacuum, the air drag vanishes and they rise to the same height. No relative motion is observed between the two intruders (except that at the end of the cycle the heavy intruder dives into the bed again). To see if Stokes drag plays any appreciable role, the intruders were put on a plate and subsequently tapped. They rose to the same height within our experimental resolution demonstrating that Stokes drag on the intruder is negligible.

Summarizing, we find that the drag on the intruder inside the bed is substantial and originates from the pressure gradient set up by the bed during the shaking cycle. In the absence of the bed, where Stokes drag is applicable, the air drag has no measurable effect on the intruder.

Huerta *et al.* [18] proposed a different model for the formation of the peak in the risetime versus ρ/ρ_m. They suggest that the peak results from a competition between convection and inertia effects, both of which should also occur in vacuum. However, in our experiments the density dependence always vanished at low pressures. We checked this result explicitly for 2 mm tapioca pearls, a medium that is similar to the 3 mm pearls used by Huerta *et al.* The peak observed at atmospheric pressure flattened out in vacuum. The reason why air is still important for these relatively large and porous media is that tapioca is a very light material ($\rho_m=1.2$ g/ml) and much more susceptible to drag forces than glass beads ($\rho_m=2.5$ g/ml) of comparable size.

The literature on granular size separation mainly deals with two systems: The single intruder on one hand and binary mixtures which separate into two phases on the other hand. In the former system the interaction is only between the intruder and the bed, while in binary mixtures the interactions between the particles that make up one species need to be taken into account as well. In a model proposed by Hong and co-workers [25] the separation of binary mixtures depends on the granular temperatures of each species. The species with the larger diameter condenses at the bottom of the container—the so-called reverse Brazil nut effect—if $D/d \geqq \rho_d/\rho_D$, where ρ_d and ρ_D are the densities of the small and large species, respectively. This model was shown to be in agreement with a recent experiment on separating binary mixtures [26] with particle diameters in the range 2–22 mm.

In order to test for the onset of interactions between multiple intruders in our system we investigated cases of up to nine intruders in a variety of initial geometrical arrangements. All intruders were placed at the same starting height in a large, rough cell ($R=6.0$ cm) with glass beads as bed material. We used $d=0.5$ and 1.0 mm beads and intruder sizes ranging from $D/d=12.5$ to 51, and density ratios ρ_d/ρ_D between 0.3 and 2. Therefore the condition derived by Hong *et al.* for the reverse Brazil nut effect to occur was always satisfied. However, none of the configurations sank. Moreover, the intruders moved as a compound with risetimes that did not show any appreciable difference to our single intruder experiment. This held independently of the initial spatial arrangement of multiple intruders. This result has two implications: If the model proposed by Hong *et al.* [25] were applicable, then many more intruders are needed to establish a granular temperature that gives rise to condensation at the bottom. Secondly, in the regime of our experiment the size ratio D/d is not the only relevant parameter and air effects clearly cannot be neglected.

IV. MODEL

The experimentally established connection between the density dependent risetimes and the presence of pressure gradients during shaking can be understood using a simple model that we develop in this section. This model takes into account the interactions between the bed, the intruder, and the air flow during each shaking cycle and enables us to deduce the net displacement of the intruder after each tap. In the next section we will incorporate the model into a simulation to provide a more quantitative comparison to our experimental results.

Each shaking cycle is divided into two parts: During part I, the bed lifts off the bottom of the cell and a gap beneath opens up. The low-pressure region formed at the bottom causes air to flow down. As a result the bed and the intruder

experience a downward force. Smaller media with lower permeability increase that air drag. The second part of the cycle starts when the gap starts to close again, the pressure gradient reverses sign and air flows upwards until the bed hits the bottom of the cell [37,38,40]. Let us now make some simplifying assumptions: We treat the bed as a porous solid with a constant packing fraction ϕ; any gap caused by relative motion between intruder and bed is immediately filled up; the pressure gradients created during the shaking cycle do not depend on the position within the bed; horizontal pressure dependence due to the presence of walls is negligibly small; finally, we do not consider convection.

Within this model the vertical pressure gradient across the bed is governed by Darcy's Law

$$\frac{\partial P}{\partial z} = \frac{\mu}{k} u, \tag{1}$$

where k is the permeability of the bed, μ the viscosity of the interstitial fluid, and u the fluid velocity outside the bed. The pressure $P(z,t)$ is a function of time and the vertical coordinate z only. Using Eq. (1) we find the drag force on the bed medium F_m and intruder F_{int},

$$F_m = \partial P/\partial z \cdot V_m = \frac{\partial P/\partial z}{\phi \cdot \rho_m} m_{\mathrm{bed}}, \tag{2}$$

$$F_{\mathrm{int}} = \oint_S P\hat{z}\vec{dS} = \partial P/\partial z \cdot V_{\mathrm{int}} = \frac{\partial P/\partial z}{\rho} m_{\mathrm{int}}. \tag{3}$$

In the last integral we used the assumption that $\partial P/\partial z$ is a function of time only. This drag term, F_{int}, has been used before to describe the effect of air on a particle in a vibrated bed [16,28,40]. Comparing F_m and F_{int}, it is clear that the bed and the intruder experience the same acceleration when $\rho/\rho_m = \phi$.

We now compare this drag force and the viscous drag acting on the intruder. The viscous drag in laminar flow is given by Stokes formula,

$$F_{\mathrm{Stokes}} = 6\pi\eta r u. \tag{4}$$

In our setup, $r = 0.0125$ m, $u \approx A(2\pi f) = 0.6$ m/s, and m_{int} ranges from 0.5 to 66.7 g, so $F_{\mathrm{Stokes}}/(m_{\mathrm{int}} \cdot g)$ ranges from 5.2×10^{-4} to 3.9×10^{-6}. Therefore, we can safely ignore simple Stokes drag on the intruder. The viscous drag on the bed has been accounted for in Darcy's Law, where the bed is treated as a continuous porous block. The intruder is also subject to the force due to pressure gradients as shown in Eq. (3). The typical gradients in our bed with 0.5 mm glass bead during the shaking cycle can be estimated from Darcy's Law (1): $\partial P/\partial z \approx 25 \times 10^3$ Pa/m using $\mu = 1.8 \times 10^{-5}$ Pa s for air and the Carman-Kozeny relation for the permeability of a random packed bed of spheres [41]

$$k = \frac{d^2(1-\phi)^3}{180\phi^2}. \tag{5}$$

Therefore $F_{\mathrm{int}}/(m_{\mathrm{int}} \cdot g)$ is between 0.31–42. Even though Stokes drag does not influence the intruder appreciably, the forces due to pressure gradients are substantial.

It is useful to estimate the effective acceleration acting on the bed in part I. The apex of an object's trajectory on which a constant drag force F_d acts and an initial velocity v_0 is given by $h_{\max} = v_0^2/(2g_{\mathrm{eff}})$, where

$$g_{\mathrm{eff}} = g\left(1 + \frac{F_d}{mg}\right) = g\left(1 + \frac{\mu u}{k\phi\rho_m g}\right) \tag{6}$$

after substituting Eq. (2).

Substituting $\rho_m = 2500$ kg/m^3 for glass, a typical packing fraction $\phi = 0.54$ and $u = 0.6$ m/s we obtain $g_{\mathrm{eff}} = 27$ m/s^2, close to the acceleration of the light intruder in Figs. 13(a) and 14 until it slows down and the kink develops. We expect the intruder at density ρ^* to have the same acceleration as well in part I, since it moves with the bed. This is indeed the case as shown in Fig. 13(a). The intruder has the same acceleration before it slows down in part II. The slow down is not as abrupt as for the light intruder.

At density $\rho^*/\rho_m = \phi$ the accelerations of the intruder and the bed are the same, so there will be no relative motion. In order to illustrate the consequences of air drag on different density intruders it is instructive to look at the two parts of the cycle for an extremely light and heavy intruder.

Part I: If $\rho \gg \rho^*$, the downward acceleration on the bed is greater than for the intruder as shown by Naylor *et al.* [22]. The intruder will push the bed above it. The closer the intruder is to the surface the less material it has to displace. If $\rho \ll \rho^*$, the intruder will be pushed against the bed below it. Two things can now happen: If the intruder is near the bottom of the bed, less material has to be displaced and the intruder can sink with respect to the bed. If the intruder is located close to the surface, the material below will block the downward motion of the intruder and it moves with the bed.

Part II: For intruders with $\rho \gg \rho^*$ the time of flight is longer than for the bed. While the bed collapses the intruder is still in the upward motion with respect to the bed. The escaping air has little effect on the intruder and the void below it is filled up with bed material. By the time the trajectory of the intruder has passed its apex the bed has almost collapsed and it will have a soft landing on the bed resulting in a net upward displacement. The light intruder with $\rho \ll \rho^*$ will be accelerated upwards with respect to the bed due to its low inertia. If it is near the bottom, it cannot displace much of the material above it. Above the crossover height, however, it has enough inertia to displace the material above and therefore will rise with respect to the bed.

The net displacement of the intruder after one shaking cycle is the sum of displacements in part I and II. Therefore, intruders with densities different from ρ^* rise faster than convection or, for the case of light intruders started initially below a crossover height, will sink. In summary our model makes the following predictions:

(1) At density $\rho^*/\rho_m = \phi$ the intruder does not move with respect to the bed. In our simplified model without convection it would stay put. In reality, however, there is always some convection and the intruder will follow whatever background flow there is in the system. If the flow is symmetric wall-driven convection, then the intruder will surface in the middle of the cylinder. In the case of the asymmetric con-

vection, the intruder will be driven to the side of the container.

(2) At all the other densities, the intruder will experience relative motion with respect to the bed due to air drag. The intruder will push the bed above or below, depending on the relative accelerations during the cycle. The dynamics between the intruder and the bed caused by air drag enable light and heavy intruders to move faster through the bed than those at ρ^*.

(3) There exists a crossover height below which light intruders with $\rho < \rho^*$ sink.

(4) The density dependence should vanish when the relative size D/d becomes small. Even though the acceleration due to the drag force on the intruder $F_{\mathrm{int}}/m_{\mathrm{int}}$ is independent of D, the absolute value of its inertia decreases with D^3. Therefore smaller intruders displace less bed than larger ones with the same acceleration. Intruders with small size ratio D/d rise with convection as is evident in Fig. 10(a). This is also the reason why Knight *et al.* [29] did not observe any deviation from convection when they measured intruder rise-times. All their intruders had a relative size $D/d \leqslant 10$.

(5) The validity of this model is independent of the phase of the sine wave excitation. In general, this is true for any excitation in which the acceleration exceeds g and therefore causes the bed to lift off. Whenever a gap opens up, the air flows downward, independent of whether the cell moves up or down at that point. Consequently, any excitation can be delineated into two phases in which the air flows down first and then up.

A consequence of these considerations is the existence of a crossover height. From symmetry arguments one would naively expect it to be in the middle of the bed. However, convection and fluidization of the upper layers cause an upwards bias in the intruder motion. Moreover, the inertia of the intruder breaks the symmetry. Despite the total impulse during the cycle due to drag being close to zero, there will still be a net movement. Even if the intruder did not collide with the bed during flight it would not return to its initial position. This is due to the different initial velocities at the beginning of part I and part II of the cycle. These factors explain why the crossover height is usually not in the middle of the bed.

Despite explaining main features of the separation mechanism the model fails to account for some of our observations. One is the decrease of ρ^* with decreasing pressure (Figs. 7 and 8). Even though $\rho^*/\rho_m \lesssim \phi$, it is unlikely that ϕ would decrease to below 0.4. One possible explanation is that the pressure gradients are not spatially uniform at lower pressures. In this case Eq. (3) would no longer hold.

Another feature of the data the model does not capture is the nonmonotonic behavior of the crossover height h_c as a function of pressure (insets of Figs. 7 and 8).

V. SIMULATION

In order to test key aspects of our model we performed a numerical simulation. In particular the computation of the pressure distribution in the bed during one shaking cycle sheds light on one main assumption in the model: the linear change of pressure with depth at all times.

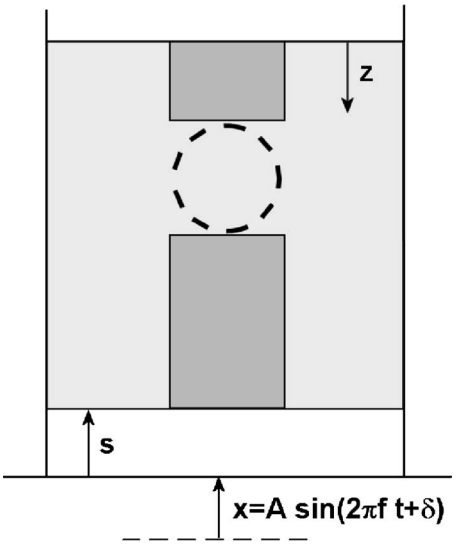

FIG. 15. Sketch of the vibrating bed indicating the variables used in the model. The dark areas above and below the intruder are the cylindrical bed volumes displaced by the intruder during the shaking cycle. s is the height of the gap between the lower edge of the bed and the cell bottom.

The starting point is the Gutman model [37,42] for the motion of a vibrated porous bed. It essentially models a porous piston in a vibrated cell subject to drag forces as the air pulsates through the bed. There is no friction between the bed and the walls and the air flow is assumed to be governed by Darcy's Law (1), as before. The model also allows for the isothermal compression of the gas [42]. Figure 15 shows a schematic view of the system and introduces the relevant variables.

The pressure $P(z,t)$ obeys the diffusion equation [41]

$$\frac{\partial P}{\partial t} = \frac{P_0 k}{\mu(1-\phi)} \frac{\partial^2 P}{\partial z^2}. \tag{7}$$

This equation together with Eq. (1) are subject to the following boundary conditions: At the top of the bed at $z=0$, the pressure $P=P_0$, where P_0 is the ambient pressure. At $z=H$, the continuity equation holds and

$$\frac{d(\rho_{\mathrm{gas}} s)}{dt} = \rho_{\mathrm{gas},0} u = -\ \rho_{\mathrm{gas},0} \frac{k}{\mu} \frac{\partial P}{\partial z}\bigg|_{z=H}, \tag{8}$$

where $\rho_{\mathrm{gas},0}$ is the density of the gas at atmospheric pressure P_0. Since $\rho_{\mathrm{gas}} \approx \rho_{\mathrm{gas},0}$ and $s(d\rho/dt) \ll \rho_{\mathrm{gas},0}(ds/dt)$ this reduces to

$$\frac{ds}{dt} = -\ \frac{k}{\mu} \frac{\partial P}{\partial z}\bigg|_{z=H}. \tag{9}$$

Note that this approximation implies that the pressure variations are small compared to the absolute pressure. In our system, the pressure varies by ≈ 4 kPa. Therefore, we require $P_0 \gg 4$ kPa.

The equation of the bed during the flight is given by

$$\frac{d^2(s+x)}{dt^2} = -g + \frac{(P|_{z=H} - P_0)}{\rho_m \phi H}, \tag{10}$$

where $x(t)=A\sin(2\pi ft+\delta)$ describes the oscillatory motion of the cell in the lab frame. The bed lifts off when the acceleration of the cell reaches $-g$. Thus, $\delta=\arcsin(1/\Gamma)$. We integrate the diffusion equation (7) numerically subject to the boundary conditions using the Crank-Nicholson scheme [43].

The first step in the simulation establishes the pressure distribution inside the bed during a shaking cycle as a function of depth and time. Also the equation of motion of the whole bed (10) is computed. We neglect any pressure redistribution due to the presence of the intruder. This would lead to small corrections that depend on the intruder geometry.

The second step determines the rise and sink time of different density intruders at a specified starting height h_s. The simulation integrates the equation of motion of three masses: The bed volumes above and below the intruder and the intruder itself (Fig. 15). These three objects ($i=1,2,3$) are subject to drag forces and their displacement y_i in the shaker frame obeys

$$\frac{d^2(s+y_i)}{dt^2} = -g + \frac{\oint_{S_i} P\hat{z}\vec{d}S}{\rho_i V_i}. \tag{11}$$

The simulation computes the net displacement after each tap, which is the difference between initial and final position of the intruder plus a small, fixed upwards displacement to account for convection. The intruder is allowed to displace the upper and lower bed volumes during flight, and after the shaking cycle any gaps are filled up to freeze the intruder in place.

In order for the intruder to sink, there must be a net downward displacement from its original position at the end of each shaking cycle: The intruder must either penetrate the material below it or, more likely, some of this material must be displaced sideways upon hitting the bottom of the cell. In order to avoid introducing more parameters and assumptions to the simulation for modeling the bed displacement we stop the simulation at this point. Nevertheless, we suggest that the region inaccessible to the simulation is where sinking is possible according to our model.

Figure 16 shows the results of the simulation for our standard system: $H=8.5$ cm, $\Gamma=5$, $f=13$ Hz, $d=0.5$ mm, $D=2.5$ cm, $P=101$ kPa and the convection displacement is 0.7 mm/tap. The latter can be obtained from the experiments as follows. From Fig. 7 we know that at ρ^* the intruder traverses 35 mm in 45 taps. Since the convection speed does not change appreciably with depth (Fig. 11), the displacement due to convection is $\approx 35/45=0.7$ mm/tap. The packing fraction was chosen to be close to the random closed pack limit, $\phi=0.63$, but any value between 0.5–0.63 yields similar results.

Comparing the simulation (Fig. 16) to the experimental data from Figs. 7 and 8 yields quantitative agreement of key features: Both the peak and the divergence in Fig. 16 occur at $\rho^*/\rho_m=0.5$ and 0.6, respectively. Even though sink times cannot be obtained in a quantitative fashion from the simulation without introducing additional parameters, the gray area in Fig. 16(b) is consistent with the sinking regime from the experiment.

Moreover, the simulated intruder trajectories closely match the high-speed measurements in Fig. 12(a): Denser intruders rise higher and the apex occurs at later times. Light intruders on the other hand, slow down in part II of the cycle.

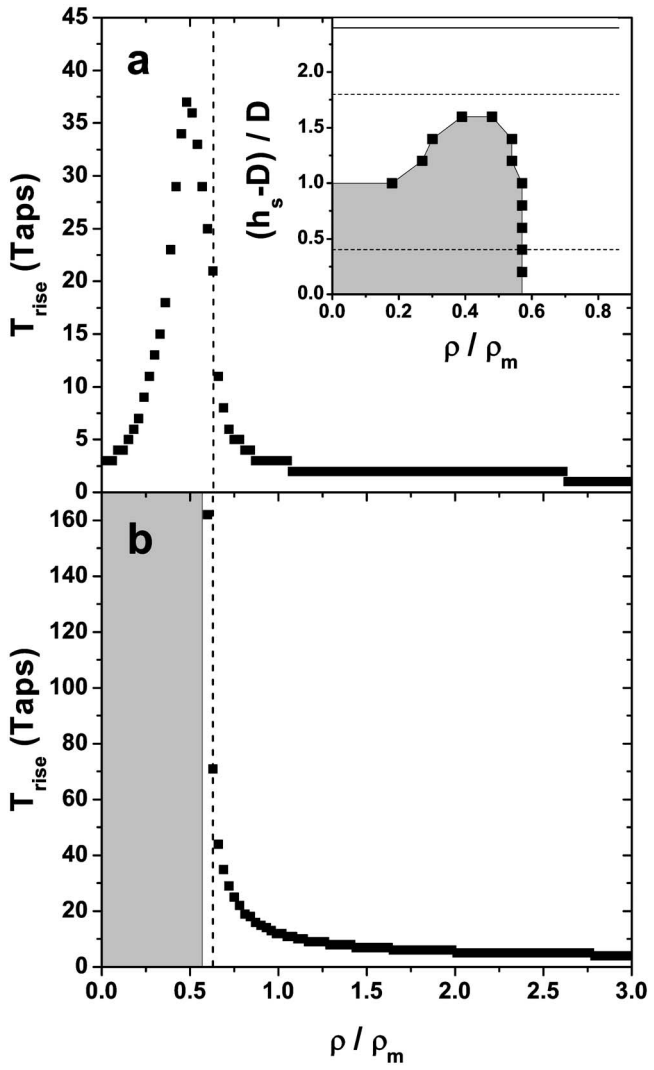

FIG. 16. Simulation results of risetime $T_{\rm rise}$ versus relative density ρ/ρ_m at two starting heights above and below the crossover height: (a) $h_s=7.0$ cm and (b) $h_s=3.5$ cm. The parameters are: $H=8.5$ cm, $f=13$ Hz, $\Gamma=5$, $\phi=0.63$ (vertical dotted line) and the convection displacement is 0.7 cm/tap. The inset in (a) shows the phase diagram of this system at atmospheric pressure. Solid and dashed lines indicate total bed height and the two starting heights in (a) and (b), respectively. The gray area indicates the region inaccessible to the simulation (see text).

This slow-down is responsible for the net displacement of the light intruder with respect to the surrounding bed. The trajectories of the light intruders cross those at ρ^* at approximately $t=0.05$ s, which agrees well with our simulation result. The kink in the simulated light intruder trajectory is caused by the intruder traversing the gap created above it in part I. In the experiment, this gap is likely to get partially filled thereby impeding the intruder motion. The simulated trajectories of the light intruder above and below the crossover height [Fig. 12(b)] agree well with the data apart from the kink due to the presence of the gap. The trajectory of the sinking intruder is only simulated until the lower bed volume hits the bottom of the cell.

The simulation of a shaking cycle stops when the entire bed hits the bottom of the cell. In the experiments, however, the intruder keeps moving past that point as shown in Fig. 12. This is because the bed dilates during flight and condenses as the bottom layers hit the cell bottom. This condensation takes approximately 0.02 s. The heavy intruder keeps moving even longer, since it is penetrating the bed due to its large inertia. These effects are not considered in our simulation and, given our results, they seem to be second order effects.

The top boundary of the gray sinking regime is not flat [inset Fig. 16(a)]. Instead it dips down at low densities. Experimentally, however, we do not observe this for the 0.5 mm glass medium. Nevertheless, Fig. 9 suggests that this dip may exist for large permeabilities.

Due to the restrictions on P_0 by virtue of the approximations made in Eq. (9), we cannot probe very low pressures in the simulation. Down to $P=40$ kPa, ρ^*/ρ_m only shifted to 0.45, which is a smaller reduction than observed in the experiment [17]. Even though the pressure change does not seem to affect ρ^* significantly, the crossover height goes up at lower pressures. Moreover, making convection stronger by choosing a higher value for the convection displacement in the simulation decreased the crossover height.

Summarizing our simulation results, we find that important parameters, such as peak and divergence position agree well with experiments. The reason why the peak does not occur exactly at ϕ is due to the fact that the pressure is not changing linearly with depth at all times. This is a key assumption in our model. The simulation shows departures from this assumption. The intruder trajectories are in good quantitative agreement with the experimental data (Fig. 12) within the limits of our simulation. We do not expect a full quantitative correspondence with the experiment due to several factors the simulation lacks. It does not account for penetration of the intruder through the bed, it lacks any fluidization during flight and the experimental excitation is not perfectly sinusoidal as assumed in the simulation. Moreover, the bed masses that are displaced are assumed to be columns, which is another idealization. Nevertheless, given the simplifying assumptions, our model captures the essential features of the Brazil nut phenomenon and qualitatively reproduces the experimentally observed phase diagrams in Figs. 7 and 8.

A nonmonotonic risetime versus density curve that peaks at $\rho^*/\rho_m \approx \phi$ has previously also been seen in a model proposed by Rhodes *et al.* [16]. These authors use an equation of motion for the intruder that includes three additional forces: two types of bed retardation and an added mass term. It requires three fitting parameters that are not directly obtainable from experiment. Our model on the other hand needs only one directly-measurable parameter, the convection displacement, which has a clear physical origin.

VI. CONCLUSIONS

The role of air in vibration-induced granular size separation can be dramatic. In media which are sufficiently small and light, air effects dominate the process of size separation and can cause intruders to sink that would rise otherwise. This process is essentially decoupled from background convection. MRI, freezing the bed with water, and high speed video measurements enabled us to study the flows inside the bed and elucidate the separation mechanism.

A key finding is that even though Stokes drag on the intruder in the absence of the bed is negligible, the drag caused by bed-induced pressure gradients is not. For 1 in. diameter intruders in 0.5 mm bed material the gradients can lead to forces several tens of times the intruders' own weight. These forces cause relative motion with respect to the bed during one shaking cycle. This leads to a phase diagram that separates rising and sinking behavior as a function of depth and pressure. Intruders with $\rho/\rho_m < \phi$ sink if started below some crossover height. Our model gives a unified description of the rising and sinking of an intruder that agrees with previous experimental results.

The air drag also causes a size and density dependence of the speed with which intruders rise or sink. We find that at $\rho^*/\rho_m \approx \phi$ the intruder moves with the convective background. Heavier intruders rise faster than convection, while lighter intruders rise or sink with respect to convection depending on their initial vertical position in the bed. This result as well as measurements of the flight trajectories of the intruder during a tap are in quantitative agreement with the model we developed.

In this model, heavy intruders rise because bed particles are held back more strongly by drag due to pressure gradients. Light intruders, on the other hand, are more easily buffeted by the air currents flowing through the bed; if placed initially near the bottom, this can push the intruder downward, whereas if placed near the top the intruder can get driven toward the upper surface. However, we cannot explain the decrease of ρ^* as the pressure is lowered in the framework of our model. This might be due to simplifying assumptions, such as constant packing fraction, lack of fluidization, and intruder penetration. Despite the fact that our model cannot account for all the rich details this experiment yields, it does unify previously disjointed pieces of data, mainly the rising and sinking of light intruders.

The air driven size separation is a nonequilibrium phenomenon. The different dynamics during the two parts of the shaking cycle explain the observed results. Even though our studies concentrated on the single intruder situation, similar considerations can be made for multi-intruders and binary mixtures where the size difference is large and the bed permeability is small.

ACKNOWLEDGMENTS

We thank N. Mueggenburg and E. Corwin for fruitful discussions and J. Rivers for help with the MRI. P.E. acknowledges the hospitality of the James Franck Institute during his stay. This work was supported by the NSF under Grant No. CTS-0405619, and under MRSEC, No. DMR-0213745 and by DOE under Contract No. W-7405-ENG-82. M.E.M. acknowledges support from the Burroughs-Wellcome Fellowship No. 1001774.

[1] J. Duran, *Sands, Powders and Grains* (Springer, New York, 2000).
[2] A. Kudrolli, Rep. Prog. Phys. **67**, 209 (2004).
[3] H. M. Jaeger, S. R. Nagel, and R. P. Behringer, Rev. Mod. Phys. **68**, 1259 (1996).
[4] R. L. Brown., J. Inst. Fuel **13**, 15 (1939).
[5] J. C. Williams, Powder Technol. **15**, 245 (1976).
[6] M. H. Cooke, J. Stephens, and J. Bridgwater, Powder Technol. **15**, 1 (1976).
[7] L. T. Fan and Y.-M. Chen, Powder Technol. **61**, 255 (1990).
[8] S. B. Savage, in *Developments in Engineering Mechanics*, edited by A. P. S. Selvadurai (Elsevier Science, Amsterdam, 1987), pp. 347–363.
[9] K. Shinohara, in *Handbook of Powder Science and Technology*, edited by M. E. Fayed and L. Ottern (van Nostrand Reinhold, New York, 1984), pp. 129–168.
[10] A. D. Rosato, K. J. Strandburg, F. Prinz, and R. H. Swendsen, Phys. Rev. Lett. **58**, 1038 (1987).
[11] T. Shinbrot and F. J. Muzzio, Phys. Rev. Lett. **81**, 4365 (1998).
[12] X. Yan, Q. Shi, M. Hou, K. Lu, and C. K. Chan, Phys. Rev. Lett. **91**, 014302 (2003).
[13] T. Shinbrot, Nature (London) **429**, 352 (2004).
[14] M. E. Möbius, B. E. Lauderdale, S. R. Nagel, and H. M. Jaeger, Nature (London) **414**, 270 (2001).
[15] M. E. Möbius, S. R. Nagel, and H. M. Jaeger, Mater. Res. Soc. Symp. Proc. **759**, 115 (2003).
[16] M. Rhodes, S. Takeuchi, K. Liffman, and K. Muniandy, Granular Matter **5**, 107 (2003).
[17] M. E. Möbius, X. Cheng, G. S. Karczmar, S. R. Nagel, and H. M. Jaeger, Phys. Rev. Lett. **93**, 198001 (2004).
[18] D. A. Huerta and J. C. Ruiz-Suárez, Phys. Rev. Lett. **92**, 114301 (2004); **93**, 069901(E) (2004).
[19] L. Trujillo and H. J. Herrmann, Physica A **330**, 519 (2003).
[20] K. Liffman *et al.*, Granular Matter **3**, 205 (2001).
[21] Y. Nahmad-Molinari, G. Canul-Chay, and J. C. Ruiz-Suárez, Phys. Rev. E **68**, 041301 (2003).
[22] M. A. Naylor, M. R. Swift, and P. J. King, Phys. Rev. E **68**, 012301 (2003).
[23] G. Gutierrez *et al.*, Europhys. Lett. **66**, 139 (2004).
[24] N. Shishodia and C. R. Wassgren, Phys. Rev. Lett. **87**, 084302 (2001).
[25] D. C. Hong, P. V. Quinn, and S. Luding, Phys. Rev. Lett. **86**, 3423 (2001).
[26] A. P. J. Breu, H.-M. Ensner, C. A. Kruelle, and I. Rehberg, Phys. Rev. Lett. **90**, 014302 (2003).
[27] N. Burtally, P. J. King, and M. R. Swift, Science **295**, 1877 (2002).
[28] P. Biswas, P. Sánchez, M. R. Swift, and P. J. King, Phys. Rev. E **68**, 050301(R) (2003).
[29] J. B. Knight, H. M. Jaeger, and S. R. Nagel, Phys. Rev. Lett. **70**, 3728 (1993).
[30] J. B. Knight *et al.*, Phys. Rev. E **54**, 5726 (1996).
[31] W. Kroll, Forsch. Geb. Ingenieurwes. **20**, 2 (1954).
[32] R. Jullien and P. Meakin, Nature (London) **344**, 425 (1990); R. Jullien, P. Meakin, and A. Pavlovitch, Phys. Rev. Lett. **69**, 640 (1992).
[33] J. Duran, J. Rajchenbach, and E. Clément, Phys. Rev. Lett. **70**, 2431 (1993).
[34] J. Duran, T. Mazozi, E. Clément, and J. Rajchenbach, Phys. Rev. E **50**, 5138 (1994).
[35] L. Vanel, A. D. Rosato, and R. N. Dave, Phys. Rev. Lett. **78**, 1255 (1997).
[36] W. Cooke, S. Warr, J. M. Huntley, and R. C. Ball, Phys. Rev. E **53**, 2812 (1996).
[37] R. G. Gutman, Trans. Inst. Chem. Eng. **54**, 174 (1976).
[38] B. Thomas and A. M. Squires, Phys. Rev. Lett. **81**, 574 (1998); Powder Technol. **100**, 200 (1998).
[39] The high-speed movies demonstrating the drag on the intruders can be found on http://jfi.uchicago.edu/~jaeger/granular2/videos/Brazil Nut videos.html
[40] H. K. Pak, E. Van Doorn, and R. P. Behringer, Phys. Rev. Lett. **74**, 4643 (1995); R. P. Behringer, E. Van Doorn, R. D. Hartley, and H. K. Pak, Granular Matter **4**, 9 (2002).
[41] P. C. Carman, *Flow of Gases through Porous Media* (Butterworth Scientific, London, 1956).
[42] R. G. Gutman and J. F. Davidson, Chem. Eng. Sci. **30**, 89 (1975).
[43] W. H. Press, B. P. Flannery, S. A. Teukolsky, and W. T. Vetterling, *Numerical Recipes in C* (Cambridge University Press, Cambridge, 1990).